Impact of the Rotation and Compactness of Progenitors on the Mass of Black Holes

Michela Mapelli[1,2,3] , Mario Spera[1,2,4,5] , Enrico Montanari[1], Marco Limongi[6,7] , Alessandro Chieffi[8,9] ,
Nicola Giacobbo[1,2,3] , Alessandro Bressan[3,10] , and Yann Bouffanais[1,2]

[1] Physics and Astronomy Department Galileo Galilei, University of Padova, Vicolo dell'Osservatorio 3, I-35122, Padova, Italy; michela.mapelli@unipd.it
[2] INFN-Padova, Via Marzolo 8, I-35131 Padova, Italy
[3] INAF-Osservatorio Astronomico di Padova, Vicolo dell'Osservatorio 5, I-35122, Padova, Italy
[4] Center for Interdisciplinary Exploration and Research in Astrophysics (CIERA), Evanston, IL 60208, USA
[5] Department of Physics & Astronomy, Northwestern University, Evanston, IL 60208, USA
[6] Istituto Nazionale di Astrofisica—Osservatorio Astronomico di Roma, Via Frascati 33, I-00040, Monteporzio Catone, Italy
[7] Kavli Institute for the Physics and Mathematics of the Universe, Todai Institutes for Advanced Study, The University of Tokyo, Kashiwa, 277-8583
(Kavli IPMU, WPI), Japan
[8] Istituto Nazionale di Astrofisica—Istituto di Astrofisica e Planetologia Spaziali, Via Fosso del Cavaliere 100, I-00133, Roma, Italy
[9] Monash Centre for Astrophysics (MoCA), School of Mathematical Sciences, Monash University, Victoria 3800, Australia
[10] SISSA, via Bonomea 265, I-34136 Trieste, Italy

Abstract

We investigate the impact of stellar rotation on the formation of black holes (BHs) by means of our population synthesis code SEVN. Rotation affects the mass function of BHs in several ways. In massive metal-poor stars, fast rotation reduces the minimum zero-age main sequence (ZAMS) mass for a star to undergo pair instability and pulsational pair instability. Moreover, stellar winds are enhanced by rotation, peeling off the entire hydrogen envelope. As a consequence of these two effects, the maximum BH mass we expect from the collapse of a rotating metal-poor star is only $\sim 45\,M_\odot$, while the maximum mass of a BH born from a nonrotating star is $\sim 60\,M_\odot$. Furthermore, stellar rotation reduces the minimum ZAMS mass for a star to collapse into a BH from ~ 18–$25\,M_\odot$ to ~ 13–$18\,M_\odot$. Finally, we have investigated the impact of different core-collapse supernova (CCSN) prescriptions on our results. While the threshold value of compactness for direct collapse and the fallback efficiency strongly affect the minimum ZAMS mass for a star to collapse into a BH, the fraction of the hydrogen envelope that can be accreted onto the final BH is the most important ingredient in determining the maximum BH mass. Our results confirm that the interplay between stellar rotation, CCSNe and pair instability plays a major role in shaping the BH mass spectrum.

Unified Astronomy Thesaurus concepts: Astrophysical black holes (98); Stellar mass black holes (1611); Stellar mass loss (1613); Computational methods (1965); Gravitational wave astronomy (675); Massive stars (732)

1. Introduction

The mass function of stellar black holes (BHs) is still an open question in astrophysics. Gravitational wave data are going to revolutionize our knowledge about BHs in the coming years: the first two observing runs of the LIGO–Virgo collaboration (LVC) led to the detection of 10 binary BHs (Abbott et al. 2019a, 2019b); few additional events were claimed by Venumadhav et al. (2019) and Zackay et al. (2019), based on a different pipeline; and several new public triggers were announced during the third observing run of the LVC, which is still ongoing. This growing population of BHs complements the sample from dynamical mass measurements in nearby X-ray binaries (Özel et al. 2010; Farr et al. 2011) and will provide us with an unique opportunity to test BH formation models.

According to our current understanding, compact object masses are strictly related to the mass evolution and the final fate of their progenitor stars. Massive stars ($\gtrsim 30\,M_\odot$) can lose a significant fraction of their initial mass by stellar winds, depending mostly (but not only) on their metallicity (Kudritzki et al. 1987; Vink et al. 2001) and luminosity (Gräfener & Hamann 2008; Vink et al. 2011). We expect that the final mass and the inner properties of a star at the onset of collapse have a strong impact on the final outcome of a core-collapse supernova (CCSN). If the final mass of the star is sufficiently large (Fryer 1999; Fryer & Kalogera 2001) and the central

compactness sufficiently high (O'Connor & Ott 2011; Ugliano et al. 2012), a star might even avoid the final explosion and collapse to a BH quietly. Based on this reasoning, the maximum mass of BHs is predicted to depend on the progenitor's metallicity, with metal-poor stars leaving more massive remnants than metal-rich ones (Heger et al. 2003; Mapelli et al. 2009, 2010, 2013; Belczynski et al. 2010; Fryer et al. 2012; Spera et al. 2015; Spera & Mapelli 2017).

This basic framework is complicated by uncertainties on CCSN models (e.g., Janka 2012, 2017; Foglizzo et al. 2015; Pejcha & Thompson 2015; Sukhbold et al. 2016; Burrows et al. 2018; Ebinger et al. 2019a, 2019b), by the existence of other explosion mechanisms, such as electron-capture supernovae (Nomoto 1984, 1987; Jones et al. 2013), pulsational pair instability supernovae (PPISNe), and pair instability supernovae (PISNe) (Fowler & Hoyle 1964; Barkat et al. 1967; Woosley et al. 2007; Woosley 2017, 2019), and by the complex physics of massive star evolution.

In particular, population synthesis models used to investigate the mass function of (single and binary) BHs (e.g., Bethe & Brown 1998; Portegies Zwart & Yungelson 1998; Belczynski et al. 2002, 2008, 2010; Mapelli et al. 2013, 2017, 2019; Mennekens & Vanbeveren 2014; Spera et al. 2015, 2019; Eldridge & Stanway 2016; Spera & Mapelli 2017; Stevenson et al. 2017, 2019; Giacobbo et al. 2018; Giacobbo & Mapelli 2018; Kruckow et al. 2018; Mapelli & Giacobbo 2018;

Eldridge et al. 2019) do not usually include stellar rotation among their ingredients. This might be a serious issue because stellar rotation can dramatically affect the evolution of the progenitor star (Dvorkin et al. 2018; Limongi & Chieffi 2018; Groh et al. 2019). Rotation has (at least) two competing effects on stellar evolution. It enhances chemical mixing (Meynet & Maeder 2005; Ekström et al. 2012; Chieffi & Limongi 2013; de Mink & Mandel 2016; Marchant et al. 2016; Mandel & de Mink 2016), leading to the development of larger stellar cores, and at the same time enhances mass loss, quenching the final stellar mass (see e.g., Limongi 2017 for a review). Stars with a He core $135 \gtrsim M_{\mathrm{He}}/M_\odot \gtrsim 64$ are expected to undergo a PISN leaving no compact remnant. Stars with $64 \gtrsim M_{\mathrm{He}}/M_\odot \gtrsim 32$ experience enhanced mass loss because of pulsational pair instability. Since stellar rotation leads to the formation of more massive He cores, especially at low metallicity where winds are quenched, the minimum zero-age main sequence (ZAMS) mass for a rotating star to undergo PISN and PPISN can be significantly smaller than the minimum ZAMS mass for a nonrotating star.

Moreover, most population synthesis codes model the outcome of a CCSN explosion based on the carbon–oxygen mass of the progenitor star, following the prescriptions in Fryer et al. (2012), but hydrodynamical simulations of CCSNe suggest that this approach might be incomplete. For example, O'Connor & Ott (2011) propose that the outcome of a CCSN, for a given equation of state, can be estimated, to the first order, by the compactness of the stellar core at bounce, defined as

$$\xi_M = \frac{M/M_\odot}{R(M)/1000\,\mathrm{km}}, \qquad (1)$$

where $R(M)$ is the radius that encloses a baryonic mass equal to M at core bounce and M is a given mass (usually $M = 2.5\,M_\odot$).

Here we present a new version of the population synthesis code SEVN (Spera et al. 2015; Spera & Mapelli 2017; Spera et al. 2019) in which we include stellar rotation by means of the FRANEC stellar evolution tracks (Limongi et al. 2000; Chieffi & Limongi 2004, 2013; Limongi & Chieffi 2006, 2018). We discuss the impact of stellar rotation on compact object mass. We also add a new simple prescription to include compactness and we compare the outcomes of CCSNe described by compactness with prescriptions from Fryer et al. (2012).

2. Methods

2.1. SEVN

SEVN's main difference with respect to most population synthesis codes is the approach to stellar evolution (Spera et al. 2015; Spera & Mapelli 2017; Spera et al. 2019). While the vast majority of population synthesis codes implement stellar evolution through the polynomial fitting formulas initially derived by Hurley et al. (2000), SEVN describes stellar evolution through look-up tables, obtained from stellar evolution tracks.[11] The look-up tables contain information on star mass and core mass, star radius and core radius, stellar metallicity, and evolutionary stages. Currently, the default tables are derived from the PARSEC stellar evolution tracks (Bressan et al. 2012; Tang et al. 2014; Chen et al. 2015; Marigo et al. 2017). In this work, we describe the implementation of

new tables derived from FRANEC (see the Section 2.2). The interpolation algorithm adopted in SEVN is already described in Spera & Mapelli (2017) and Spera et al. (2019). The main advantage of using look-up tables with respect to polynomial fitting formulas is that stellar evolution in SEVN can be updated very easily by changing the current set of look-up tables with a new one, while polynomial fitting formulas are bound to the stellar evolution model they were extracted from.

Binary evolution is implemented in SEVN following the prescriptions by Hurley et al. (2002). We include a treatment of tides, decay by gravitational wave emission, mass transfer, and common envelope as already discussed in Spera et al. (2019). The main novelty with respect to Hurley et al. (2002) consists of the description of common envelope and stellar mergers. Thanks to the interpolation algorithm, the mass and the stellar type of the outcome of a common envelope or a stellar merger are derived from the look-up tables directly, without the need for a collision matrix or other fitting formulas.

Here, we describe the new tables derived from FRANEC and the updates to the description of CCSN outcomes in SEVN.

2.2. FRANEC Stellar Evolution Tracks

The stellar models adopted in this paper have been computed by means of the latest release of the FRANEC code. Here, we summarize their main features, while we refer to Limongi & Chieffi (2018) for a full description of the models and the code.[12] The initial masses are 13, 15, 20, 25, 30, 40, 60, 80, and $120\,M_\odot$, the initial metallicities are [Fe/H] = 0, −1, −2, −3, and the initial equatorial rotation velocities are 0, 150, and $300\,\mathrm{km\,s^{-1}}$. We adopt the solar composition from Asplund et al. (2009), corresponding to a total heavy element mass fraction of $Z_\odot \sim 0.0135$. At metallicities lower than solar we consider a scaled solar distribution with the exception of C, O, Mg, Si, S, Ar, Ca, and Ti, for which we assume [C/Fe] = 0.18, [O/Fe] = 0.47, [Mg/Fe] = 0.27, [Si/Fe] = 0.37, [S/Fe] = 0.35, [Ar/Fe] = 0.35, [Ca/Fe] = 0.33, and [Ti/Fe] = 0.23, consistent with the observations of unevolved metal-poor stars (Cayrel et al. 2004; Spite et al. 2005). As a consequence, the total metallicities corresponding to [Fe/H] = −1, −2, −3 are $Z \sim 3 \times 10^{-3}$, 3×10^{-4}, 3×10^{-5}, respectively. The initial velocities were chosen to roughly span the range of observed values (Dufton et al. 2006; Hunter et al. 2008; Ramírez-Agudelo et al. 2017).

The nuclear network, fully coupled to the equations for the stellar structure as well as to the various kinds of mixing, includes 335 isotopes in total, from H to ^{209}Bi, linked by more than 3000 nuclear reactions. This network is well suited to properly follow all the stable and explosive nuclear burning stages of massive stars.

Mass loss is taken into account following different prescriptions for the various evolutionary stages, e.g., Vink et al. (2000, 2001) for the blue supergiant phase ($T_{\mathrm{eff}} > 12,000\,\mathrm{K}$), de Jager et al. (1988) for the red supergiant phase ($T_{\mathrm{eff}} < 12,000\,\mathrm{K}$) and Nugis & Lamers (2000) for the Wolf–Rayet phase. The dust driven wind occurring during the red supergiant phase has been included following the prescriptions of van Loon et al. (2005). Mass loss is enhanced, in rotating models, according to Heger et al. (2000). When the star approaches the

---

[11] COMBINE (Kruckow et al. 2018) is the only other binary population synthesis code (besides SEVN) that adopts look-up tables and has been used to study binary compact objects.

[12] The main properties of these models, together to their final yields, are available at the webpage http://orfeo.iaps.inaf.it. More specific details about the models may be provided upon request.

Eddington limit, mass loss is modeled as described in Limongi & Chieffi (2018).

Rotation is treated as described in Chieffi & Limongi (2013) and Limongi & Chieffi (2018). Two main rotation driven instabilities are taken into account, i.e., meridional circulation and turbulent shear. The efficiency of the mixing induced by these two phenomena has been calibrated by requiring the fit to a subset of stars (taken from the Large Magellanic Cloud samples of the FLAMES survey, Hunter et al. 2009) for which both the surface N abundance and the projected rotation velocity are available.

2.3. Core-collapse Supernovae (CCSNe)

SEVN includes five different models to describe the outcome of CCSNe: the rapid and delayed models presented in Fryer et al. (2012), the prescriptions adopted in STARTRACK (Belczynski et al. 2008), the compactness criterion (O'Connor & Ott 2011), and the two-parameter criterion by Ertl et al. (2016). The first three models depend only on the carbon–oxygen mass after carbon burning and on the presupernova mass of the star, the fourth model depends also on the compactness $\xi_{2.5}$, defined in Equation (1) (assuming $M = 2.5 M_\odot$), while the fifth model depends on the enclosed mass at a dimensionless entropy per nucleon $s = 4$ (M_4) and the mass gradient at the same location (μ_4).

2.3.1. Compactness Model

In the previous version of SEVN, the criterion based on compactness and the two-parameter criterion were implemented in a non-self-consistent way, because the table of compactness $\xi_{2.5}$ and that of M_4 and μ_4 were calculated through the MESA code (Paxton et al. 2011, 2013, 2015), while stellar evolution was derived from PARSEC. Here, we update the treatment of compactness in a self-consistent way. In fact, compactness can be calculated directly from FRANEC models, because they are evolved up to the onset of core collapse.[13]

Limongi & Chieffi (2018) have shown that there is a strong correlation between compactness and carbon–oxygen mass at the onset of collapse (see their Figure 21) and this correlation is not significantly affected by stellar rotation. Thus, in our new version of SEVN, we interpolate compactness among stellar models by using the following fitting formula:

$$\xi_{2.5} = a + b \left(\frac{m_{CO}}{1\,M_\odot} \right)^c, \qquad (2)$$

where $a = 0.55$, $b = -1.1$, $c = -1.0$. Figure 1 shows the fit reported in Equation (2) overlaid on the FRANEC data.

O'Connor & Ott (2011) suggest that progenitors with $\xi_{2.5} > 0.45$ most likely form BHs without an explosion, while Horiuchi et al. (2014) suggest a lower threshold value ($\xi_{2.5} \gtrsim 0.2$). In this work, we adopt $\xi_{2.5} = 0.3$ as a threshold (unless explicitly stated otherwise) and we simply assume that progenitors with $\xi_{2.5} \leqslant 0.3$ form a neutron star (NS) by CCSN explosion, while progenitors with $\xi_{2.5} > 0.3$ form a BH by direct collapse.

Several recent papers claim that $\xi_{2.5}$ does not show a monotonic trend with the CO core (Sukhbold et al. 2018 and
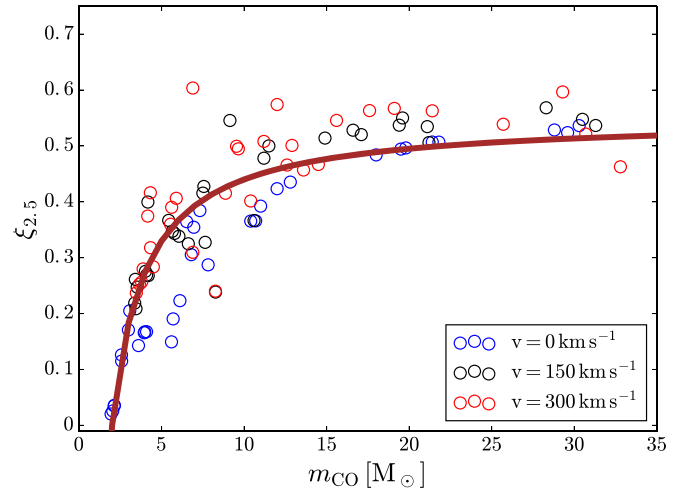
---

[13] O'Connor & Ott (2011) adopt compactness at bounce, but Ugliano et al. (2012) show that compactness at the onset of collapse is consistent with compactness at bounce and is much easier to estimate. Hereafter, we refer to compactness at the onset of collapse.

Figure 1. Compactness $\xi_{2.5}$ as a function of the carbon–oxygen core mass (m_{CO}) at the onset of collapse for the FRANEC evolutionary tracks with rotation $v = 0$, 150, and 300 km s^{-1} (blue, black and red circles, respectively). The dark red line overlaid on the data is the fit described in Equation (2).

references therein), but rather has a complicated trend, with several localized branches and multivalued solutions. This result is still a matter of debate. We are studying this problem in detail and will discuss our results in a forthcoming paper. For this reason, and for the purposes of the present paper, here we adopt a conservative approach based on the results presented in Limongi & Chieffi (2018).

The compactness criterion allows us to discriminate between the formation of a NS (if the progenitor explodes) and that of a BH (if the progenitor collapses directly). When the progenitor explodes leaving a NS, the mass of the NS is assigned randomly, following a Gaussian distribution with mean $\langle m_{NS} \rangle = 1.33 M_\odot$ and dispersion $\sigma_{NS} = 0.09 M_\odot$, based on the distribution of observed NSs in binary NS systems (Özel & Freire 2016).

When the progenitor undergoes a direct collapse, the mass of the BH is derived as

$$m_{BH} = m_{He} + f_H (m_{fin} - m_{He}), \qquad (3)$$

where m_{fin} and m_{He} are the total mass and the He core mass of the star at the onset of collapse, respectively (the He core, by definition, includes also heavier elements inside the He core radius), while f_H is a free parameter which can assume values from 0 to 1. The presence of f_H accounts for the uncertainty about the collapse of the H envelope (if the progenitor star retains a H envelope to the very end). Some studies (e.g., Nadezhin 1980; Lovegrove & Woosley 2013; Sukhbold et al. 2016; Fernández et al. 2018) stress that is quite unlikely that the H envelope collapses entirely, even during a direct collapse, because it is loosely bound. In the following, we consider the two extreme cases in which $f_H = 0$ (the H envelope is completely lost) and $f_H = 0.9$ (90% of the H envelope collapses). Equation (3) is a toy model and does not intend to capture the complex physics of direct collapse. However, if we consider the two extreme cases with $f_H = 0$ and $f_H = 0.9$, we are able to bracket the main uncertainties on direct collapse.

In the compactness model, we assume that the efficiency of fallback is negligible, following recent hydrodynamical simulations (e.g., Ertl et al. 2016).

2.3.2. Rapid Model

In this work, we compare the new compactness criterion implemented in SEVN with the rapid CCSN model by Fryer et al. (2012), which assumes that the explosion occurs <250 ms after bounce. In the rapid model, the mass of the compact object is $m_{rem} = m_{proto} + m_{fb}$, where $m_{proto} = 1\,M_\odot$ is the mass of the protocompact object and $m_{fb} = f_{fb}\,(m_{fin} - m_{proto})$ is the mass accreted by fallback. In the previous expression, f_{fb} is the fractional fallback parameter, defined as in Fryer et al. (2012).

In the rapid CCSN formalism, the maximum NS mass is $2\,M_\odot$, while the minimum BH mass is $5\,M_\odot$. This result strongly depends on the assumptions about fallback. In contrast, our compactness-based model cannot predict a maximum NS mass, because the mass of the NS is derived from an observational distribution (Özel & Freire 2016).

We stress that none of the prescriptions currently adopted in the literature to infer the mass of compact objects (including the rapid model and the compactness-based models adopted in this work) are sufficient to capture the complexity of CCSN physics (see, e.g., Burrows et al. 2018, 2019; Vartanyan et al. 2019). The aim of our study is to compare different CCSN prescriptions and to quantify the uncertainties on the BH mass spectrum that arise from a different choice of these simplified prescriptions.

2.4. PPISNe and PISNe

SEVN includes a treatment for PISNe and PPISNe as described in Spera & Mapelli (2017), based on the results of Woosley (2017). In particular, if the He core mass is $135 \geqslant m_{He}/M_\odot \geqslant 64$, the star undergoes a PISN and leaves no compact object. If the He core mass is $64 > m_{He}/M_\odot \geqslant 32$, the star undergoes pulsational pair instability and the final mass of the compact object is calculated as $m_{rem} = \alpha_P\,m_{no\,PPI}$, where $m_{no\,PPI}$ is the mass of the compact object we would have obtained if we had not included pulsational pair instability in our analysis (just CCSN), and α_P is a fitting parameter described in the Appendix.

3. Results

3.1. Impact of Rotation on BH Masses

Figures 2 and 3 show the mass of compact objects as a function of the ZAMS mass of their progenitor stars for different CCSN models (rapid, compactness with $\xi_{2.5} = 0.3$ and $f_H = 0$, and compactness with $\xi_{2.5} = 0.3$ and $f_H = 0.9$). We show the results we obtain with FRANEC stellar evolution tables for three initial equatorial velocities of the progenitor stars: $v = 0$, 150, and $300\,km\,s^{-1}$. For comparison, we show also the results of PARSEC stellar evolution tables with $v = 0\,km\,s^{-1}$.

From these figures the strong impact of rotation on the minimum ZAMS mass for BH formation, regardless of the progenitor's metallicity, is apparent. The minimum progenitor mass to collapse to a BH is $m_{ZAMS} \sim 13\text{–}18\,M_\odot$ for rotating stars and $m_{ZAMS} \sim 18\text{–}25\,M_\odot$ for nonrotating stars (with a mild dependence on the CCSN model, see Table 1). This happens because stars with $10 \lesssim m_{ZAMS}/M_\odot \lesssim 30$ are not particularly affected by stellar winds, regardless of their metallicity. Thus, angular momentum is not efficiently removed by mass loss and rotation has enough time to induce

chemical mixing, leading to the growth of the stellar core. This shifts the threshold between explosion and direct collapse toward lower ZAMS masses.

Furthermore, Figures 2 and 3 show that stellar rotation has a strong impact on the (pulsational) pair instability window for metal-poor stars ($Z = 0.0003$, 0.00003), independent of the assumed CCSN model. The most metal-poor rotating models ($Z = 0.0003$, 0.00003) undergo PISN and PPISN at significantly lower ZAMS masses than the nonrotating models (e.g., $m_{PPISN} \sim 50\,M_\odot$ and $\sim 70\,M_\odot$ for rotating and nonrotating models, respectively, see Table 1). Again, this happens because chemical mixing leads to significantly larger He cores in rotating metal-poor stars. We note that there are no significant differences between $v = 150\,km\,s^{-1}$ and $v = 300\,km\,s^{-1}$.

We now go through different metallicities, to discuss how the effect of stellar rotation changes with Z. In metal-poor stars ($Z \leqslant 0.0003$), stellar winds are relatively inefficient over the entire mass spectrum, even for rotating stars. Thus, the main effect of rotation is always the enhancement of chemical mixing, leading to the growth of the stellar core. This has the two main consequences we discussed above, i.e., a smaller minimum ZAMS mass for BH formation and a smaller minimum ZAMS mass for PPISNe and PISNe.

In contrast, at intermediate metallicity ($Z = 0.003$, approximately $1/5$ of the solar metallicity), the impact of rotation is different for stars with $m_{ZAMS} \lesssim 30\,M_\odot$ and $m_{ZAMS} \gtrsim 30\,M_\odot$. If $m_{ZAMS} \lesssim 30\,M_\odot$, stellar winds are not particularly efficient, even in rotating models. Thus, rotating stars develop larger cores and end their life with higher compactness than nonrotating stars. The main consequence of this is that the minimum progenitor mass to collapse to a BH is smaller for rotating stars than for nonrotating stars. In contrast, if $m_{ZAMS} \gtrsim 30\,M_\odot$, stellar winds are efficient at $Z = 0.003$ and they are significantly enhanced by rotation. Because of enhanced mass loss, the He core of rotating stars tends to be smaller than the He core of nonrotating stars. As a consequence of this, at $Z = 0.003$ the minimum ZAMS mass to enter the PPISN regime is slightly lower for nonrotating models ($m_{PPISN} \sim 66\text{–}68\,M_\odot$ for $v = 0\,km\,s^{-1}$, Table 1) than for rotating models ($m_{PPISN} \sim 80\,M_\odot$ for $v = 300\,km\,s^{-1}$, Table 1), with an opposite behavior with respect to more metal-poor stars. Stars with $m_{ZAMS} \leqslant 120\,M_\odot$ and $Z = 0.003$ do not develop He cores $>64\,M_\odot$, thus they do not enter the PISN regime.

Finally, metal-rich stars ($Z = 0.0135 \sim Z_\odot$) with $m_{ZAMS} \leqslant 30\,M_\odot$ behave similarly to metal-poor stars: they are only mildly affected by mass loss; hence, rotating stars grow larger He cores than nonrotating stars, causing the minimum ZAMS mass for BH formation to shift to lower values in rotating models. In contrast, stellar winds are so efficient in metal-rich stars with $m_{ZAMS} \gtrsim 30\,M_\odot$ that they do not enter either the PPISN or PISN window, regardless of their rotation speed (with the exception of the PARSEC model, which undergoes PPISNe at $m_{ZAMS} \gtrsim 94\,M_\odot$). At high Z, stellar rotation does not significantly affect the maximum BH mass, which is $\sim 16\text{–}24\,M_\odot$, regardless of the assumed CCSN model.

3.2. Impact of CCSN Model on BH Masses

Figure 2 shows the mass of compact objects we obtain assuming the rapid CCSN model described in Fryer et al. (2012). In contrast, Figure 3 is based on the compactness criterion. By considering these different models, we want to
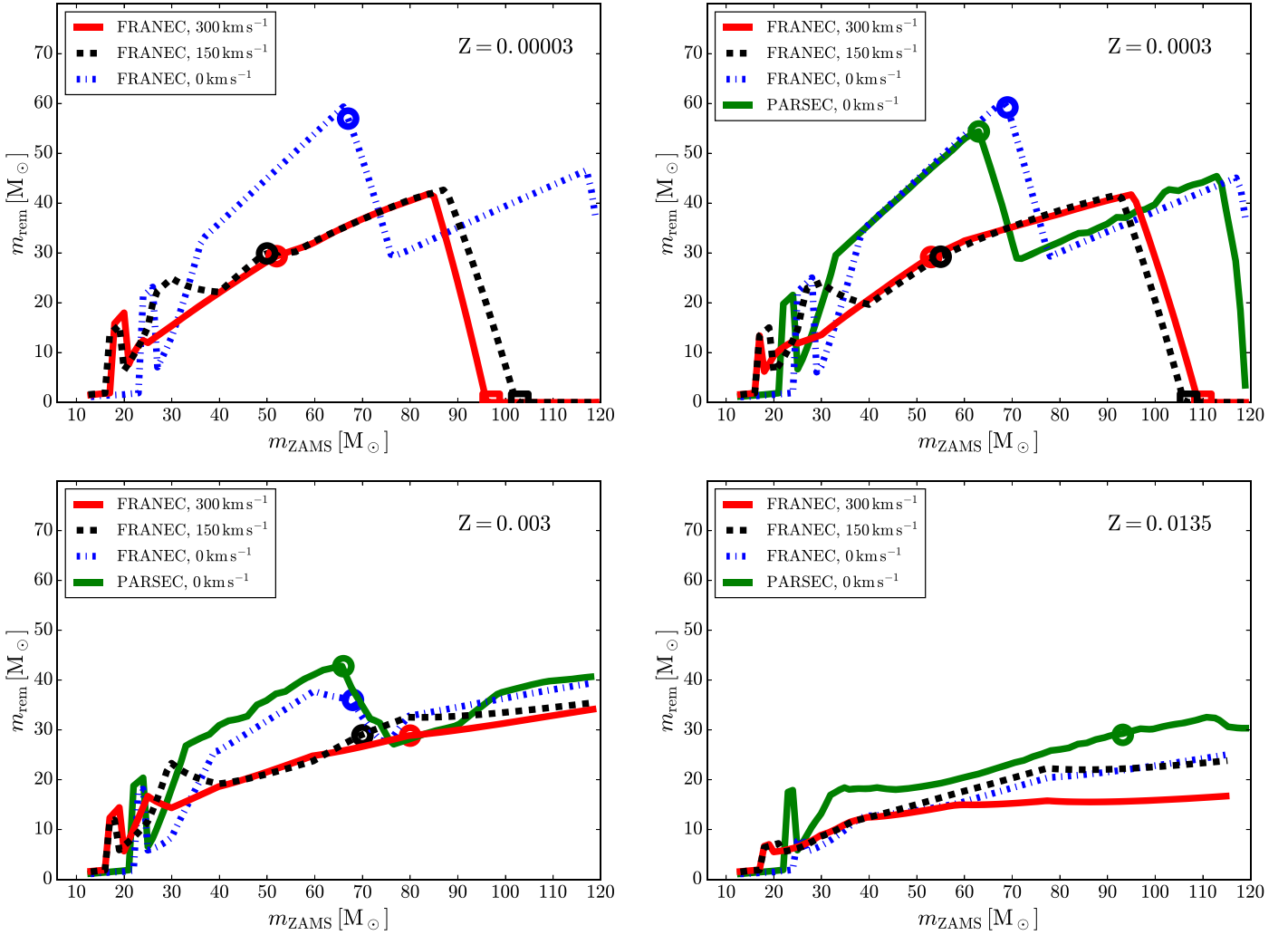
Figure 2. Estimated mass of the compact object ($m_{\rm rem}$) as a function of the zero-age main sequence (ZAMS) mass of the progenitor star ($m_{\rm ZAMS}$). The outcome of CCSNe is described by the rapid model (Fryer et al. 2012). From top to bottom and from left to right: $Z = 0.00003, 0.0003, 0.003$ and 0.0135. Red solid line: stellar evolution is described by FRANEC (Limongi & Chieffi 2018) with initial equatorial rotation speed $v = 300$ km s^{-1}. Black dashed line: FRANEC (Limongi & Chieffi 2018) with $v = 150$ km s^{-1}. Blue dotted–dashed line: FRANEC (Limongi & Chieffi 2018) with $v = 0$ km s^{-1}. Green solid line: stellar evolution is described by PARSEC (Bressan et al. 2012). We do not have PARSEC models with metallicity $Z = 0.00003$. Open circles (squares): ZAMS mass at which the star develops a He core $m_{\rm He} = 32\,M_\odot$ ($m_{\rm He} = 64\ M_\odot$), corresponding to the minimum mass to undergo PPISN (PISN).

quantify the uncertainty on BH mass derived from CCSN prescriptions.

The main sources of uncertainty are the amount of fallback, the minimum value of the compactness (or carbon–oxygen mass) required for direct collapse, and the fate of the hydrogen envelope (if any). The rapid model by Fryer et al. (2012) assumes that fallback can be efficient (mass accreted by fallback $m_{\rm fb} \geqslant 0.2\,M_\odot$) and that stars with a carbon–oxygen core mass $m_{\rm CO} \geqslant 11\,M_\odot$ collapse to a BH directly, including their hydrogen envelope (if any). In contrast, in the compactness model we assume no fallback at all and we require that stars with compactness $\xi_{2.5} \geqslant 0.3$ collapse to a BH directly. In the case of direct collapse with the compactness criterion, if $f_{\rm H} = 0.0$ ($f_{\rm H} = 0.9$) we assume that the hydrogen envelope does not collapse (90% of the hydrogen envelope collapses) to a BH.

The main difference between the rapid model and the compactness model, which manifests regardless of stellar rotation and metallicity, is the minimum ZAMS mass to form a BH (Table 1). This difference arises mostly from the adopted threshold for direct collapse. In fact, direct collapse happens in

the rapid model if $m_{\rm CO} \geqslant 11\,M_\odot$, which (according to Equation (2)) corresponds to the compactness threshold $\xi_{2.5} \geqslant 0.45$. By increasing the threshold for direct collapse from $\xi_{2.5} = 0.3$ to $\xi_{2.5} = 0.45$, the compactness models produce approximately the same minimum ZAMS mass for BH formation as the rapid model.

Another feature of the rapid model which does not show up in the compactness-based models, regardless of stellar metallicity and rotation, is the complex behavior of BH mass for $m_{\rm ZAMS} \lesssim 40\,M_\odot$. This is a consequence of the sophisticated fitting formulas for fallback derived from Fryer et al. (2012).

If $m_{\rm ZAMS} \gtrsim 40\,M_\odot$, metallicity and rotation matter, as we have seen in the previous section. If stellar metallicity is high ($Z = 0.0135$) and $m_{\rm ZAMS} \gtrsim 40\,M_\odot$, the mass of BHs in the rapid model and in the compactness models have a remarkably similar behavior. The reason is that stellar winds are very efficient in massive stars with $Z = 0.0135$ (almost independently of rotation) and remove the entire envelope, leveling the differences among the considered models.

In contrast, if stellar metallicity is low ($Z \leqslant 0.003$) and $m_{\rm ZAMS} \gtrsim 40\,M_\odot$, the initial rotation becomes the crucial
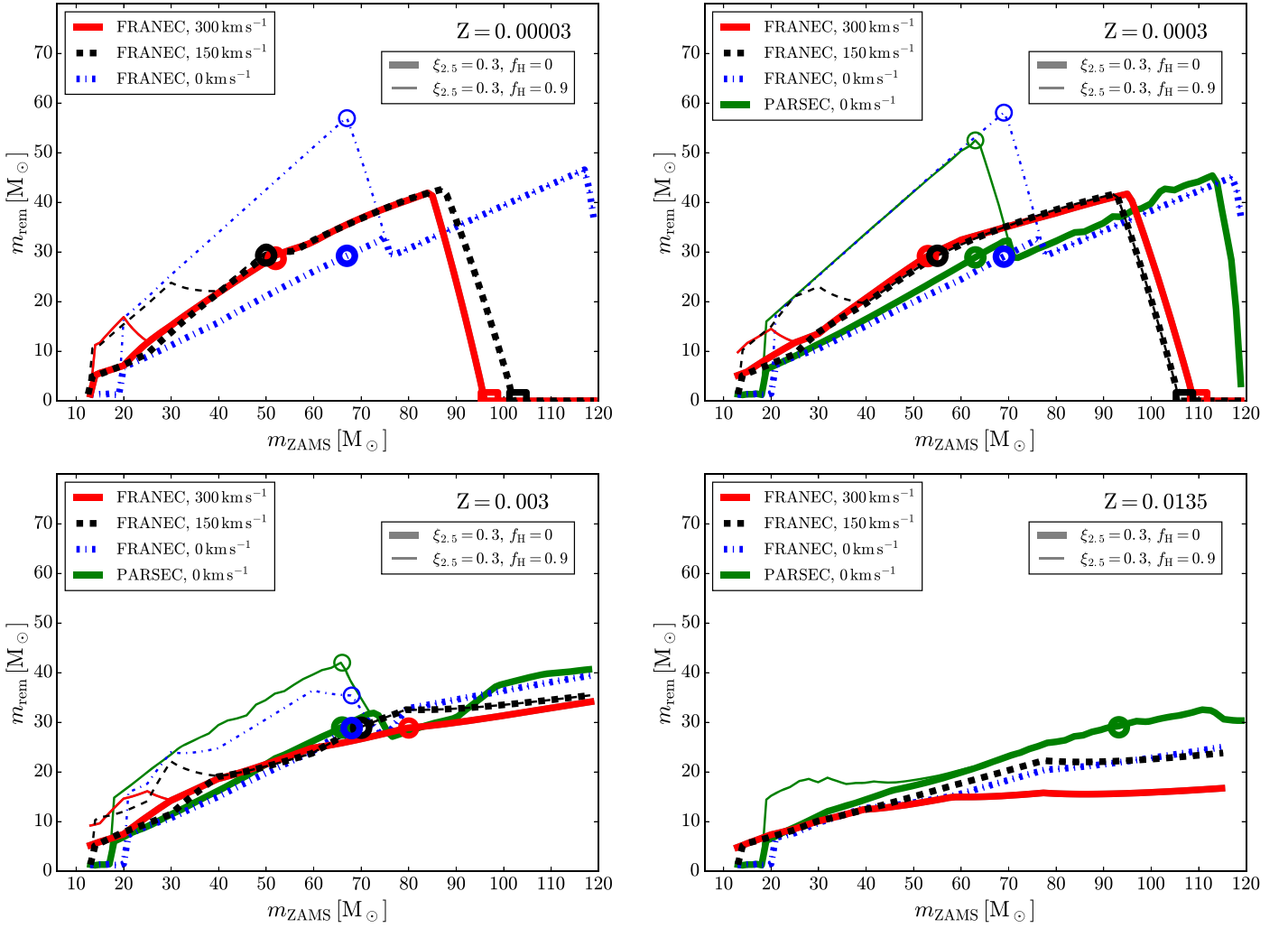
Figure 3. Same as Figure 2, but CCSNe are described with the compactness criterion. Thick lines: we assume $\xi_{2.5} = 0.3$ and $f_H = 0.0$; thin lines: we assume $\xi_{2.5} = 0.3$ and $f_H = 0.9$ (see Section 2.3.1). If the thin lines are not visible, it means that they overlap with the thick lines perfectly.

ingredient. If the star rotates, the minimum ZAMS mass for PPISN and PISN decreases significantly (see Section 3.1) and stellar winds are efficient even at low metallicity. The combination of these two effects removes the hydrogen envelope and even a fraction of the He core. For this reason, the rapid model and the two compactness models are indistinguishable for rotating stars with $Z \leqslant 0.003$ and $m_{ZAMS} \gtrsim 40\,M_\odot$.

If the star does not rotate, the BH mass for $40 \lesssim m_{ZAMS}/M_\odot \lesssim 80$ and $Z \leqslant 0.0003$ dramatically depends on the collapse of the H envelope, because the star retains a large portion of its hydrogen envelope until the final stages. Models assuming that most of the H envelope collapses (i.e., the rapid model and the compactness model with $f_H = 0.9$) predict a BH mass $m_{BH} \sim 60\,M_\odot$, almost twice as large as that expected from the compactness model with $f_H = 0$ in this range of ZAMS masses. Finally, nonrotating stars with $m_{ZAMS} \gtrsim 80\,M_\odot$ eject their H envelope entirely. Thus, the three CCSN models predict similar BH masses for extremely massive metal-poor nonrotating stars.

In summary, if we look at the maximum BH mass, rotating models predict $m_{BH,max} \leqslant 45\,M_\odot$ (originating from stars with $m_{ZAMS} \sim 90–100\,M_\odot$ and $Z \leqslant 0.0003$, regardless of the CCSN model. In contrast, nonrotating models predict $m_{BH,max} \sim 60\,M_\odot$

(originating from stars with $m_{ZAMS} \sim 60–70\,M_\odot$ and $Z \leqslant 0.0003$) if the H envelope is assumed to collapse, and $m_{BH,max} \sim 45–50\,M_\odot$ (originating from stars with $m_{ZAMS} \sim 110–120\,M_\odot$ and $Z \leqslant 0.0003$) if the H envelope is assumed to be ejected. These conclusions depend on the adopted description of PPISNe and PISNe (from Spera & Mapelli 2017).

3.3. Impact of Rotation, CCSN Model and Metallicity on BH Mass Function

For each considered metallicity, for each rotation speed, and for each CCSN model separately, we have generated a set of 10^5 single stars distributed according to a Kroupa initial mass function (IMF; i.e., $dN/dm \propto m^{-\alpha}$ with $\alpha = 2.3$, Kroupa 2001), with a minimum ZAMS mass $m_{min} = 13\,M_\odot$ and a maximum ZAMS mass $m_{max} = 120\,M_\odot$.

Figure 4 shows the mass function of compact objects for the three considered rotation speeds, for three metallicities ($Z = 0.00003$ is not shown because it is almost indistinguishable from $Z = 0.0003$) and for the three CCSN models. Note that the NS population is severely incomplete, because the minimum ZAMS mass currently available in the FRANEC tracks is $m_{ZAMS} = 13\,M_\odot$. Smaller masses will be included in follow-up works.

Table 1
Most Relevant Masses

Stellar Evolution	CCSN	v (km s^{-1})	Z	$m_{ZAMS,min}$ ($M_\odot$)	m_{PPISN} ($M_\odot$)	m_{PISN} ($M_\odot$)	$m_{BH,max}$ ($M_\odot$)
FRANEC	rapid	300	0.00003	18	52	97	42
FRANEC	rapid	300	0.0003	17	53	110	42
FRANEC	rapid	300	0.003	17	80	⋯	34
FRANEC	rapid	300	0.0135	18	⋯	⋯	16
FRANEC	rapid	150	0.00003	17	50	103	43
FRANEC	rapid	150	0.0003	17	55	107	42
FRANEC	rapid	150	0.003	17	70	⋯	35
FRANEC	rapid	150	0.0135	18	⋯	⋯	23
FRANEC	rapid	0	0.00003	24	67	⋯	59
FRANEC	rapid	0	0.0003	25	69	⋯	60
FRANEC	rapid	0	0.003	23	68	⋯	39
FRANEC	rapid	0	0.0135	25	⋯	⋯	24
PARSEC	rapid	0	0.0003	22	63	⋯	54
PARSEC	rapid	0	0.003	22	66	⋯	43
PARSEC	rapid	0	0.0135	23	94	⋯	33
FRANEC	$\xi_{2.5} = 0.3, f_H = 0$	300	0.00003	14	52	97	42
FRANEC	$\xi_{2.5} = 0.3, f_H = 0$	300	0.0003	⩽13	53	110	42
FRANEC	$\xi_{2.5} = 0.3, f_H = 0$	300	0.003	⩽13	80	⋯	34
FRANEC	$\xi_{2.5} = 0.3, f_H = 0$	300	0.0135	⩽13	⋯	⋯	16
FRANEC	$\xi_{2.5} = 0.3, f_H = 0$	150	0.00003	13	50	103	43
FRANEC	$\xi_{2.5} = 0.3, f_H = 0$	150	0.0003	14	55	107	42
FRANEC	$\xi_{2.5} = 0.3, f_H = 0$	150	0.003	14	70	⋯	35
FRANEC	$\xi_{2.5} = 0.3, f_H = 0$	150	0.0135	14	⋯	⋯	23
FRANEC	$\xi_{2.5} = 0.3, f_H = 0$	0	0.00003	20	67	⋯	47
FRANEC	$\xi_{2.5} = 0.3, f_H = 0$	0	0.0003	21	69	⋯	45
FRANEC	$\xi_{2.5} = 0.3, f_H = 0$	0	0.003	21	68	⋯	39
FRANEC	$\xi_{2.5} = 0.3, f_H = 0$	0	0.0135	21	⋯	⋯	24
PARSEC	$\xi_{2.5} = 0.3, f_H = 0$	0	0.0003	19	63	⋯	45
PARSEC	$\xi_{2.5} = 0.3, f_H = 0$	0	0.003	18	66	⋯	41
PARSEC	$\xi_{2.5} = 0.3, f_H = 0$	0	0.0135	19	94	⋯	33
FRANEC	$\xi_{2.5} = 0.3, f_H = 0.9$	300	0.00003	14	52	97	42
FRANEC	$\xi_{2.5} = 0.3, f_H = 0.9$	300	0.0003	⩽13	53	110	42
FRANEC	$\xi_{2.5} = 0.3, f_H = 0.9$	300	0.003	⩽13	80	⋯	34
FRANEC	$\xi_{2.5} = 0.3, f_H = 0.9$	300	0.0135	⩽13	⋯	⋯	16
FRANEC	$\xi_{2.5} = 0.3, f_H = 0.9$	150	0.00003	13	50	103	43
FRANEC	$\xi_{2.5} = 0.3, f_H = 0.9$	150	0.0003	14	55	107	42
FRANEC	$\xi_{2.5} = 0.3, f_H = 0.9$	150	0.003	14	70	⋯	35
FRANEC	$\xi_{2.5} = 0.3, f_H = 0.9$	150	0.0135	14	⋯	⋯	23
FRANEC	$\xi_{2.5} = 0.3, f_H = 0.9$	0	0.00003	20	67	⋯	57
FRANEC	$\xi_{2.5} = 0.3, f_H = 0.9$	0	0.0003	21	69	⋯	58
FRANEC	$\xi_{2.5} = 0.3, f_H = 0.9$	0	0.003	21	68	⋯	39
FRANEC	$\xi_{2.5} = 0.3, f_H = 0.9$	0	0.0135	21	⋯	⋯	24
PARSEC	$\xi_{2.5} = 0.3, f_H = 0.9$	0	0.0003	19	63	⋯	52
PARSEC	$\xi_{2.5} = 0.3, f_H = 0.9$	0	0.003	18	66	⋯	42
PARSEC	$\xi_{2.5} = 0.3, f_H = 0.9$	0	0.0135	19	94	⋯	33

Note. Column (1): Stellar evolution tables (from FRANEC or PARSEC). Column (2): model for CCSN outcome (see Section 2.3). Column (3): initial rotation speed of progenitor stars. Column (4): progenitor's metallicity. Column (5): minimum ZAMS mass to collapse to a BH (instead of producing a NS). Column (6): minimum ZAMS mass to undergo PPISN (m_{PPISN}). Column (7): minimum ZAMS mass to undergo PISN (m_{PISN}). Column (8): maximum BH mass ($m_{BH,max}$).

In general, the mass function of single BHs can be approximated with a power law, but the slope of the power law depends on metallicity, rotation speed, and on the assumed CCSN prescription. If we make a linear fit of $\log_{10} PDF = \mathcal{D} \log_{10} m_{rem} + \mathcal{G}$ across our models, we find a preferred value of $\mathcal{D} \approx -0.5$, with a very large scatter. Binary evolution can change this scaling dramatically and will be included in a follow-up study.

The main differences among all the considered models are the number of NSs and the minimum mass of BHs. Because of the difference in the minimum ZAMS mass to form a BH (see Sections 3.1 and 3.2), stars with $v = 300$ km s^{-1} and minimum mass $m_{ZAMS} = 13\,M_\odot$ adopting a compactness-based CCSN

criterion do not form NSs, regardless of their metallicity. For these extremely fast rotating models to produce NSs, we need to assume a significantly higher $\xi_{2.5}$ threshold.

The minimum BH mass spans from $\sim 4.5\,M_\odot$ to $\sim 15\,M_\odot$, depending on the CCSN prescription (the compactness-based model with $f_H = 0.9$ produces significantly larger minimum BH masses at low metallicity) and on metallicity (metal-rich populations tend to produce BHs with a smaller minimum BH mass). The maximum BH mass dramatically depends not only on metallicity, but also on rotation (BHs with mass $m_{rem} \gtrsim 60\,M_\odot$ form only from nonrotating models).

At solar metallicity, the three CCSNe models and the three rotation speeds produce very similar BH populations (almost
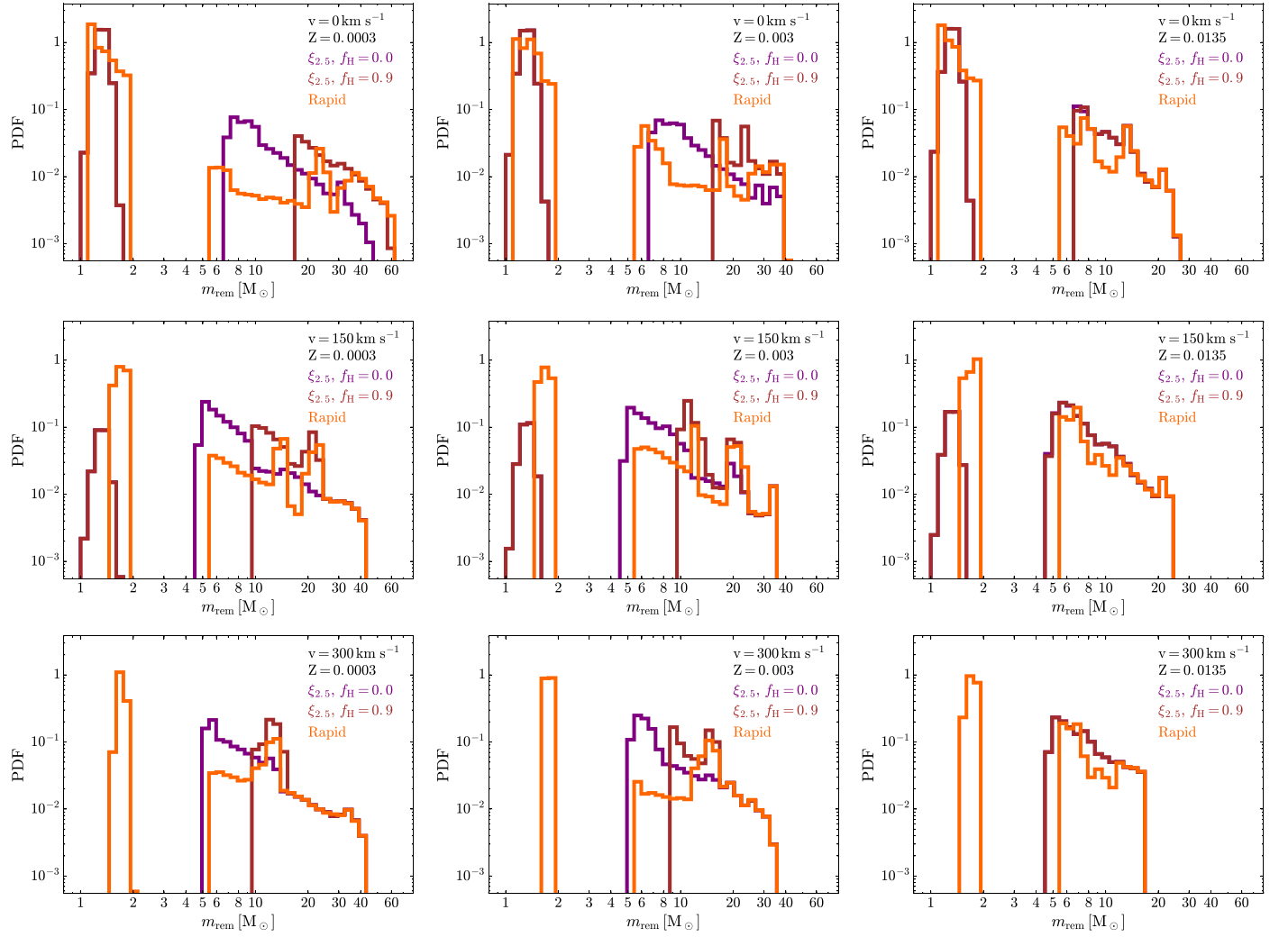
Figure 4. Probability distribution functions (PDFs) of compact object masses. We assume a Kroupa (2001) IMF for the progenitor stars with a minimum mass $m_{\rm min} = 13\,M_\odot$ and a maximum mass $m_{\rm max} = 120\,M_\odot$. Orange lines: rapid model for CCSNe (Fryer et al. 2012); purple lines: compactness criterion with $\xi_{2.5} = 0.3$ and $f_{\rm H} = 0$; dark red lines: compactness criterion with $\xi_{2.5} = 0.3$ and $f_{\rm H} = 0.9$. At $Z = 0.0135$ the purple line is nearly invisible, because it overlaps with the dark red line. Upper row: $v = 0\,{\rm km\,s^{-1}}$; middle row: $v = 150\,{\rm km\,s^{-1}}$; lower row: $v = 300\,{\rm km\,s^{-1}}$. Left column: $Z = 0.0003$; middle column: $Z = 0.003$; right column: $Z = 0.0135$.

identical in the case of the two compactness-based models). The reason is that stellar winds peel off massive stars, regardless of their initial rotation velocity and of the assumed CCSN model. In contrast, at lower metallicities the differences between the three CCSN models become important.

In this section, we assumed that stars in the same stellar population have the same initial rotation speed. This is clearly a simplistic assumption because stars might form with different initial speeds. Data of stellar rotation in the Milky Way show that stellar speeds should be distributed according to a Gaussian with an average speed $\sim$200 km s^{-1} and dispersion $\sim$100 km s^{-1} (Dufton et al. 2006). In follow-up studies we will consider a distribution of initial stellar rotation velocities.

3.4. Comparison with Previous Work

Figures 2 and 3 show that there is not much difference between PARSEC models and FRANEC models with $v = 0\,{\rm km\,s^{-1}}$ when implemented inside SEVN and treated with the same model for CCSNe, PISNe and PPISNe. It is worth noting that while the typical difference in the maximum BH mass between FRANEC and PARSEC is $\sim$10% at low

metallicity, the difference becomes $\sim$27% at solar metallicity ($Z = 0.0135$, see Table 1). This is explained with a different treatment of mass loss and different assumptions for chemical abundances.

Figure 5 compares the mass spectrum of compact objects we derived in this study (considering only FRANEC tracks and accounting for the uncertainties induced by the CCSN model with a shaded area) with the mass spectrum obtained in previous studies, as a function of the ZAMS mass. In particular, we plot the mass spectrum from Spera & Mapelli (2017), hereafter SM2017, from Giacobbo & Mapelli (2018), hereafter GM2018, and from Limongi & Chieffi (2018), hereafter LC2018. We also consider a version of BSE (Hurley et al. 2000, 2002) that includes the same stellar wind, PISN and PPISN prescriptions as STARTRACK (Belczynski et al. 2016), hereafter B2016.

Our results are similar to the mass spectrum obtained with MOBSE (GM2018), although the maximum BH mass in MOBSE ($m_{\rm BH,max} \sim 65\,M_\odot$ at $Z = 0.0003$) is $\sim$8% higher than the maximum mass we obtain with SEVN. Metal-poor stars with $m_{\rm ZAMS} \sim 40$–$80\,M_\odot$ seem to retain a more generous portion of
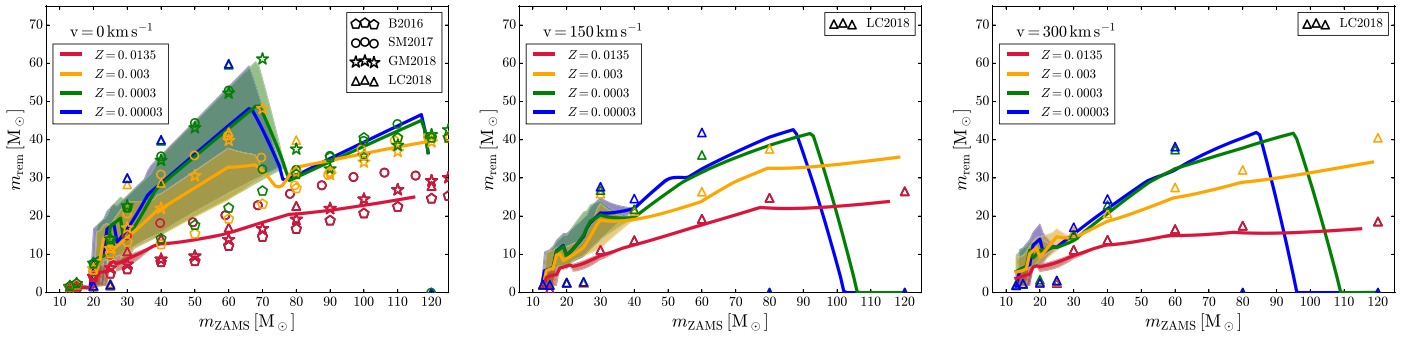
Figure 5. Mass of the compact object as a function of the progenitor's ZAMS mass for the main models we have considered, in comparison with some previous studies. Left: rotation velocity $v = 0$ km s^{-1}. Middle: $v = 150$ km s^{-1}. Right: $v = 300$ km s^{-1}. The solid lines show the mean value of m_{rem} we obtain by averaging over the three CCSN models considered in this study, while the shaded areas show the maximum differences between the three CCSN models. Open triangles (LC2018): R model from Limongi & Chieffi (2018). Open stars (GM2018): compact object mass predicted by MOBSE (Giacobbo & Mapelli 2018), adopting the delayed CCSN model by Fryer et al. (2012). Open circles (SM2017): compact object mass estimated with SEVN (Spera & Mapelli 2017), adopting the delayed CCSN and the PARSEC stellar tracks (Bressan et al. 2012). Open pentagons (B2016): compact object mass estimated with BSE (Hurley et al. 2002), adopting the same stellar winds, PPISN and PPISN model as STARTRACK (Belczynski et al. 2016). In all panels and for all symbols and lines, red: progenitor's metallicity $Z = 0.0135$; orange: $Z = 0.003$; green: $Z = 0.0003$; blue: $Z = 0.00003$.

their hydrogen envelope at collapse when integrated with MOBSE. Our results are also broadly consistent with SM2017 for metal-poor progenitors, while at $Z = 0.0135$ SM2017 predict ∼20%–30% larger BH masses (up to ∼33 $M_\odot$), explained by the fact that SM2017 adopt PARSEC tracks. The models labeled as B2016 predict a maximum BH mass ∼40 $M_\odot$, significantly smaller than our model with $f_H = 0.9$ and similar to our model with H envelope ejection ($f_H = 0$). However, B2016 assume that the H envelope, when present, collapses with the rest of the star. In their model, metal-poor stars with $m_{ZAMS} \sim 40$–$80\,M_\odot$ lose their H envelope almost completely for the different treatment of luminous blue variable stellar winds and of pulsational pair instability.

LC2018 adopt the same FRANEC tracks we use here. Figure 5 shows their model R which assumes that stars with $m_{ZAMS} \leqslant 25\,M_\odot$ explode as CCSNe, while stars with $m_{ZAMS} > 25\,M_\odot$ collapse to a BH directly, with $m_{rem} = m_{fin}$ (no mass ejection). Thus, the triangles shown in Figure 5 represent the upper limit to BH masses we can obtain with FRANEC if $m_{ZAMS} > 25\,M_\odot$.

Finally, several previous studies investigate the impact of stellar rotation on PPISNe and PISNe (Chatzopoulos & Wheeler 2012a, 2012b; Yoon et al. 2012; Yusof et al. 2013; Takahashi et al. 2018; Uchida et al. 2019). Our main findings agree with their results: (i) the minimum ZAMS mass to undergo a PPISN and a PISN lowers significantly if stellar rotation is accounted for (Chatzopoulos & Wheeler 2012a), and (ii) rotating models of massive stars lose their entire hydrogen-rich envelopes by enhanced mass loss (Yusof et al. 2013).

4. Conclusions

We have investigated the impact of rotation and compactness on the mass of black holes (BHs), by implementing rotating stellar evolution models (Limongi & Chieffi 2018) into our population synthesis code SEVN (Spera et al. 2015, 2019; Spera & Mapelli 2017).

Rotation has two major effects on BH formation. First, rotation reduces the minimum ZAMS mass for a star to collapse into a BH from ∼18–25 $M_\odot$ to ∼13–18 $M_\odot$ (according to the assumed CCSN prescriptions), because intermediate mass ($m_{ZAMS} \sim 13$–$20\ M_\odot$) rotating stars develop a larger

carbon–oxygen core and a higher compactness than nonrotating stars.

Second, rotation reduces the maximum BH mass from metal-poor progenitors. This result comes from two combined effects: (i) rotation increases stellar wind efficiency; thus, rotating metal-poor ($Z = 0.00003$–0.0003) stars with $m_{ZAMS} \sim 40$–$80\,M_\odot$ lose their H envelope entirely, while nonrotating metal-poor stars preserve most of it; (ii) chemical mixing induced by rotation increases the mass of the He core, reducing the minimum ZAMS mass for PPISNe and PISNe to happen.

If we assume that the entire final mass of a star (including its residual H envelope) can collapse to a BH directly, the maximum BH mass from nonrotating stars is ∼60 $M_\odot$, while the maximum BH mass from fast rotating stars is ∼45 $M_\odot$.

Besides rotation, the mass of BHs is also strongly affected by the assumed CCSN model, especially by the amount of fallback, by the adopted threshold for direct collapse (based on $\xi_{2.5}$ or on m_{CO}), and by the different fraction of H envelope that is able to collapse (f_H).

In particular, the minimum ZAMS mass for a star to form a BH depends on the assumed threshold of compactness $\xi_{2.5}$ (larger values of the threshold leading to higher minimum ZAMS masses) and on the efficiency of fallback.

The maximum BH mass that we expect from nonrotating metal-poor ($Z = 0.00003$–0.0003) stars depends wildly on the assumed CCSN prescription: if we assume that the residual H envelope participates in the collapse, the maximum BH mass is up to ∼60 $M_\odot$, approximately 1.5 times higher than if we assume that only the He core is able to collapse. This assumption is not important for metal-poor massive rotating stars and for metal-rich (both rotating and nonrotating) stars, because stellar winds remove their H envelope entirely, leveling these differences.

Here, we consider only single stars. In future works, we will investigate how binary evolution and star cluster dynamics affect our conclusions. We anticipate that close binary evolution should lead to a further stripping of the H envelope, affecting the maximum BH mass (see, e.g., Giacobbo & Mapelli 2018). On the other hand, star cluster dynamics can lead to the formation of binary BHs that incorporate the most massive BHs formed from single star evolution and from the

merger of massive binaries (e.g., Mapelli 2016; Di Carlo et al. 2019), making the final scenario even more complex.

The methodology we presented here might be applied to estimate upper limits on BH spins. For all our models we find an upper limit to the final spin close to maximally rotating BHs. However, our models do not include mechanisms for efficient angular momentum dissipation, such as the Tayler–Spruit dynamo (Spruit 2002; Fuller et al. 2019). Efficient angular momentum transport can lead to significantly lower BH spins ($a_{BH} \lesssim 0.1$), as described in several works (e.g., Heger et al. 2005; Belczynski et al. 2017; Fuller & Ma 2019; Qin et al. 2019). In a follow-up study, we will apply different models of angular momentum transport to our methodology.

Overall, we confirm that both stellar rotation and supernova prescriptions have a crucial impact on the mass function of BHs. This result provides a key to interpret future gravitational wave data and to constrain stellar evolution and CCSN mechanisms.

Appendix
Fitting Formula for PPISNe and PISNe

When PISNe and PPISNe are effective, we derive the mass of the compact object as $m_{rem} = \alpha_P m_{no\ PPI}$, where $m_{no\ PPI}$ is the mass of the compact remnant we would obtain without PPISN/PISN. First, we define the following quantities

$$\mathcal{F} \equiv \frac{m_{He}}{m_{fin}}, \quad \mathcal{K} \equiv 0.67000\mathcal{F} + 0.10000,$$
$$\mathcal{S} \equiv 0.52260\mathcal{F} - 0.52974. \tag{4}$$

We then express α_P as a function of $\mathcal{F}$, $\mathcal{S}$, $\mathcal{K}$ and m_{He}:

$$\alpha_P = \begin{cases} 1 & \text{if } m_{He} \leqslant 32 M_\odot, \ \forall \mathcal{F}, \ \forall \mathcal{S} \\ 0.2(\mathcal{K} - 1)m_{He} + 0.2(37 - 32\mathcal{K}) & \text{if } 32 < m_{He}/M_\odot \leqslant 37, \ \mathcal{F} < 0.9, \ \forall \mathcal{S} \\ \mathcal{K} & \text{if } 37 < m_{He}/M_\odot \leqslant 60, \ \mathcal{F} < 0.9, \ \forall \mathcal{S} \\ \mathcal{K}(16.0 - 0.25 m_{He}) & \text{if } 60 < m_{He}/M_\odot < 64, \ \mathcal{F} < 0.9, \ \forall \mathcal{S} \\ \mathcal{S}(m_{He} - 32) + 1 & \text{if } m_{He} \leqslant 37 M_\odot, \ \mathcal{F} \geqslant 0.9, \ \forall \mathcal{S} \\ 5\mathcal{S} + 1 & \text{if } 37 < m_{He}/M_\odot \leqslant 56, \ \mathcal{F} \geqslant 0.9, \ 5\mathcal{S} + 1 < 0.82916 \\ (-0.1381\mathcal{F} + 0.1309)(m_{He} - 56) + 0.82916 & \text{if } 37 < m_{He}/M_\odot \leqslant 56, \ \mathcal{F} \geqslant 0.9, \ 5\mathcal{S} + 1 \geqslant 0.82916 \\ -0.103645 m_{He} + 6.63328 & \text{if } 56 < m_{He}/M_\odot < 64, \ \mathcal{F} \geqslant 0.9, \ \forall \mathcal{S} \\ 0 & \text{if } 64 \leqslant m_{He}/M_\odot < 135, \ \forall \mathcal{F}, \ \forall \mathcal{S} \\ 1 & \text{if } m_{He} \geqslant 135 M_\odot, \ \forall \mathcal{F}, \ \forall \mathcal{S}. \end{cases} \tag{5}$$

These fits are the same as we adopted in Spera & Mapelli (2017), but here we fix some typos of Appendix B of Spera & Mapelli (2017) (these typos did not affect the results of Spera & Mapelli 2017, because the code contained the correct equations).

ORCID iDs

Michela Mapelli ⓘ https://orcid.org/0000-0001-8799-2548
Mario Spera ⓘ https://orcid.org/0000-0003-0930-6930
Marco Limongi ⓘ https://orcid.org/0000-0003-0636-7834
Alessandro Chieffi ⓘ https://orcid.org/0000-0002-3589-3203
Nicola Giacobbo ⓘ https://orcid.org/0000-0002-8339-0889
Alessandro Bressan ⓘ https://orcid.org/0000-0002-7922-8440
Yann Bouffanais ⓘ https://orcid.org/0000-0003-3462-0366

References

Abbott, B. P., Abbott, R., Abbott, T. D., et al. 2019a, PhRvX, 9, 031040
Abbott, B. P., Abbott, R., Abbott, T. D., et al. 2019b, ApJL, 882, L24
Asplund, M., Grevesse, N., Sauval, A. J., & Scott, P. 2009, ARA&A, 47, 481
Barkat, Z., Rakavy, G., & Sack, N. 1967, PhRvL, 18, 379
Belczynski, K., Bulik, T., Fryer, C. L., et al. 2010, ApJ, 714, 1217
Belczynski, K., Heger, A., Gladysz, W., et al. 2016, A&A, 594, A97
Belczynski, K., Kalogera, V., & Bulik, T. 2002, ApJ, 572, 407
Belczynski, K., Kalogera, V., Rasio, F. A., et al. 2008, ApJS, 174, 223
Belczynski, K., Klencki, J., Fields, C. E., et al. 2017, arXiv:1706.07053
Bethe, H. A., & Brown, G. E. 1998, ApJ, 506, 780
Bressan, A., Marigo, P., Girardi, L., et al. 2012, MNRAS, 427, 127
Burrows, A., Radice, D., & Vartanyan, D. 2019, MNRAS, 485, 3153
Burrows, A., Vartanyan, D., Dolence, J. C., Skinner, M. A., & Radice, D. 2018, SSRv, 214, 33
Cayrel, R., Depagne, E., Spite, M., et al. 2004, A&A, 416, 1117
Chatzopoulos, E., & Wheeler, J. C. 2012a, ApJ, 748, 42
Chatzopoulos, E., & Wheeler, J. C. 2012b, ApJ, 760, 154
Chen, Y., Bressan, A., Girardi, L., et al. 2015, MNRAS, 452, 1068
Chieffi, A., & Limongi, M. 2004, ApJ, 608, 405
Chieffi, A., & Limongi, M. 2013, ApJ, 764, 21
de Jager, C., Nieuwenhuijzen, H., & van der Hucht, K. A. 1988, A&AS, 72, 259
de Mink, S. E., & Mandel, I. 2016, MNRAS, 460, 3545
Di Carlo, U. N., Giacobbo, N., Mapelli, M., et al. 2019, MNRAS, 487, 2947
Dufton, P. L., Smartt, S. J., Lee, J. K., et al. 2006, A&A, 457, 265
Dvorkin, I., Uzan, J.-P., Vangioni, E., & Silk, J. 2018, MNRAS, 479, 121
Ebinger, K., Curtis, S., Fröhlich, C., et al. 2019a, ApJ, 870, 1
Ebinger, K., Curtis, S., Ghosh, S., et al. 2019b, arXiv:1910.08958
Ekström, S., Georgy, C., Eggenberger, P., et al. 2012, A&A, 537, A146
Eldridge, J. J., & Stanway, E. R. 2016, MNRAS, 462, 3302
Eldridge, J. J., Stanway, E. R., & Tang, P. N. 2019, MNRAS, 482, 870
Ertl, T., Janka, H.-T., Woosley, S. E., Sukhbold, T., & Ugliano, M. 2016, ApJ, 818, 124

Farr, W. M., Sravan, N., Cantrell, A., et al. 2011, ApJ, 741, 103
Fernández, R., Quataert, E., Kashiyama, K., & Coughlin, E. R. 2018, MNRAS, 476, 2366
Foglizzo, T., Kazeroni, R., Guilet, J., et al. 2015, PASA, 32, e009
Fowler, W. A., & Hoyle, F. 1964, ApJS, 9, 201
Fryer, C. L. 1999, ApJ, 522, 413
Fryer, C. L., Belczynski, K., Wiktorowicz, G., et al. 2012, ApJ, 749, 91
Fryer, C. L., & Kalogera, V. 2001, ApJ, 554, 548
Fuller, J., & Ma, L. 2019, ApJL, 881, L1
Fuller, J., Piro, A. L., & Jermyn, A. S. 2019, MNRAS, 485, 3661
Giacobbo, N., & Mapelli, M. 2018, MNRAS, 480, 2011
Giacobbo, N., Mapelli, M., & Spera, M. 2018, MNRAS, 474, 2959
Gräfener, G., & Hamann, W.-R. 2008, A&A, 482, 945
Groh, J. H., Ekström, S., Georgy, C., et al. 2019, A&A, 627, A24
Heger, A., Fryer, C. L., Woosley, S. E., Langer, N., & Hartmann, D. H. 2003, ApJ, 591, 288
Heger, A., Langer, N., & Woosley, S. E. 2000, ApJ, 528, 368
Heger, A., Woosley, S. E., & Spruit, H. C. 2005, ApJ, 626, 350
Horiuchi, S., Nakamura, K., Takiwaki, T., Kotake, K., & Tanaka, M. 2014, MNRAS, 445, L99
Hunter, I., Brott, I., Langer, N., et al. 2009, A&A, 496, 841
Hunter, I., Lennon, D. J., Dufton, P. L., et al. 2008, A&A, 479, 541
Hurley, J. R., Pols, O. R., & Tout, C. A. 2000, MNRAS, 315, 543
Hurley, J. R., Tout, C. A., & Pols, O. R. 2002, MNRAS, 329, 897
Janka, H.-T. 2012, ARNPS, 62, 407
Janka, H.-T. 2017, ApJ, 837, 84
Jones, S., Hirschi, R., Nomoto, K., et al. 2013, ApJ, 772, 150
Kroupa, P. 2001, MNRAS, 322, 231
Kruckow, M. U., Tauris, T. M., Langer, N., Kramer, M., & Izzard, R. G. 2018, MNRAS, 481, 1908
Kudritzki, R. P., Pauldrach, A., & Puls, J. 1987, A&A, 173, 293
Limongi, M. 2017, Supernovae from Massive Stars (Cham: Springer), 513
Limongi, M., & Chieffi, A. 2006, ApJ, 647, 483
Limongi, M., & Chieffi, A. 2018, ApJS, 237, 13
Limongi, M., Straniero, O., & Chieffi, A. 2000, ApJS, 129, 625
Lovegrove, E., & Woosley, S. E. 2013, ApJ, 769, 109
Mandel, I., & de Mink, S. E. 2016, MNRAS, 458, 2634
Mapelli, M. 2016, MNRAS, 459, 3432
Mapelli, M., Colpi, M., & Zampieri, L. 2009, MNRAS, 395, L71
Mapelli, M., & Giacobbo, N. 2018, MNRAS, 479, 4391
Mapelli, M., Giacobbo, N., Ripamonti, E., & Spera, M. 2017, MNRAS, 472, 2422
Mapelli, M., Giacobbo, N., Santoliquido, F., & Artale, M. C. 2019, MNRAS, 487, 2
Mapelli, M., Ripamonti, E., Zampieri, L., Colpi, M., & Bressan, A. 2010, MNRAS, 408, 234
Mapelli, M., Zampieri, L., Ripamonti, E., & Bressan, A. 2013, MNRAS, 429, 2298

Marchant, P., Langer, N., Podsiadlowski, P., Tauris, T. M., & Moriya, T. J. 2016, A&A, 588, A50
Marigo, P., Girardi, L., Bressan, A., et al. 2017, ApJ, 835, 77
Mennekens, N., & Vanbeveren, D. 2014, A&A, 564, A134
Meynet, G., & Maeder, A. 2005, A&A, 429, 581
Nadezhin, D. K. 1980, Ap&SS, 69, 115
Nomoto, K. 1984, ApJ, 277, 791
Nomoto, K. 1987, ApJ, 322, 206
Nugis, T., & Lamers, H. J. G. L. M. 2000, A&A, 360, 227
O'Connor, E., & Ott, C. D. 2011, ApJ, 730, 70
Özel, F., & Freire, P. 2016, ARA&A, 54, 401
Özel, F., Psaltis, D., Narayan, R., & McClintock, J. E. 2010, ApJ, 725, 1918
Paxton, B., Bildsten, L., Dotter, A., et al. 2011, ApJS, 192, 3
Paxton, B., Cantiello, M., Arras, P., et al. 2013, ApJS, 208, 4
Paxton, B., Marchant, P., Schwab, J., et al. 2015, ApJS, 220, 15
Pejcha, O., & Thompson, T. A. 2015, ApJ, 801, 90
Portegies Zwart, S. F., & Yungelson, L. R. 1998, A&A, 332, 173
Qin, Y., Marchant, P., Fragos, T., Meynet, G., & Kalogera, V. 2019, ApJL, 870, L18
Ramírez-Agudelo, O. H., Sana, H., de Koter, A., et al. 2017, A&A, 600, A81
Spera, M., & Mapelli, M. 2017, MNRAS, 470, 4739
Spera, M., Mapelli, M., & Bressan, A. 2015, MNRAS, 451, 4086
Spera, M., Mapelli, M., Giacobbo, N., et al. 2019, MNRAS, 485, 889
Spite, M., Cayrel, R., Plez, B., et al. 2005, A&A, 430, 655
Spruit, H. C. 2002, A&A, 381, 923
Stevenson, S., Sampson, M., Powell, J., et al. 2019, ApJ, 882, 121
Stevenson, S., Vigna-Gómez, A., Mandel, I., et al. 2017, NatCo, 8, 14906
Sukhbold, T., Ertl, T., Woosley, S. E., Brown, J. M., & Janka, H.-T. 2016, ApJ, 821, 38
Sukhbold, T., Woosley, S. E., & Heger, A. 2018, ApJ, 860, 93
Takahashi, K., Yoshida, T., & Umeda, H. 2018, ApJ, 857, 111
Tang, J., Bressan, A., Rosenfield, P., et al. 2014, MNRAS, 445, 4287
Uchida, H., Shibata, M., Takahashi, K., & Yoshida, T. 2019, ApJ, 870, 98
Ugliano, M., Janka, H.-T., Marek, A., & Arcones, A. 2012, ApJ, 757, 69
van Loon, J. T., Cioni, M. R. L., Zijlstra, A. A., & Loup, C. 2005, A&A, 438, 273
Vartanyan, D., Burrows, A., & Radice, D. 2019, MNRAS, 489, 2227
Venumadhav, T., Zackay, B., Roulet, J., Dai, L., & Zaldarriaga, M. 2019, arXiv:1904.07214
Vink, J. S., de Koter, A., & Lamers, H. J. G. L. M. 2000, A&A, 362, 295
Vink, J. S., de Koter, A., & Lamers, H. J. G. L. M. 2001, A&A, 369, 574
Vink, J. S., Muijres, L. E., Anthonisse, B., et al. 2011, A&A, 531, A132
Woosley, S. E. 2017, ApJ, 836, 244
Woosley, S. E. 2019, ApJ, 878, 49
Woosley, S. E., Blinnikov, S., & Heger, A. 2007, Natur, 450, 390
Yoon, S. C., Dierks, A., & Langer, N. 2012, A&A, 542, A113
Yusof, N., Hirschi, R., Meynet, G., et al. 2013, MNRAS, 433, 1114
Zackay, B., Venumadhav, T., Dai, L., Roulet, J., & Zaldarriaga, M. 2019, PhRvD, 100, 023007